

Dust envelopes around RV Tauri stars

A. V. Raveendran^{1*} and A. N. Other^{2*†}

¹*Indian Institute of Astrophysics, Bangalore 560034, India*

²*Building, Institute, Street Address, City, Code, Country*

Accepted 1988 December 15. Received 1988 December 14; in original form 1988 October 11

ABSTRACT

In the *IRAS* [12]–[25], [25]–[60] colour–colour diagram, RV Tauri stars are found to populate cooler temperature regions ($T < 600$ K), distinctly different from those occupied by the oxygen and carbon Miras. The *IRAS* fluxes are consistent with the dust density in the envelope varying as the inverse square of the radial distance, implying that the grain formation processes in these objects are most probably continuous and not sporadic. It is found that the spectroscopic subgroups A and B are well separated in the far-infrared two-colour diagram, with group B objects having systematically cooler dust envelopes. We interpret this as being due to a difference in the nature of grains, including the chemical composition, in the two cases.

Key words: circumstellar matter – infrared: stars.

1 INTRODUCTION

It has been well established that RV Tauri variables possess infrared emission far in excess of their expected blackbody continuum, arising from their extended cool dust envelopes (Gerhz & Woolf 1970; Gerhz 1972; Gerhz & Ney 1972). Recently, Lloyd Evans (1985) and Goldsmith et al. (1987) have given detailed descriptions of the near-infrared properties of RV Tauri stars. In this paper we present an analysis of the *IRAS* data of RV Tauri stars with the help of the far-infrared two-colour diagram and a grid computed using a simple model of the dust envelope. Such two-colour plots have already been employed extensively by several investigators to study the circumstellar envelopes around oxygen-rich and carbon-rich objects which are in the late stages of stellar evolution (Hacking et al. 1985; Zuckerman & Dyck 1986; van der Veen & Habing 1988; Willems & de Jong 1988).

Table 1 summarizes the basic data on the 17 objects detected at 60 μm . Apart from the *IRAS* identification and the flux densities at 12-, 25-, 60- and 100- μm wavebands, it gives the spectroscopic groups of Preston et al. (1963), the light-curve classes of Kukarkin et al. (1969) and the periods of light variation. The list, which contains about 20 per cent of all the known RV Tauri stars, is essentially the same as that given by Jura (1986). The spectroscopic subgroups are from either Preston et al. (1963) or Lloyd Evans (1985).

2 DESCRIPTION OF THE ENVELOPE MODEL

If we assume that the dust grains in the envelope are predominantly of the same kind and are in thermal equilibrium, the luminosity at frequency ν in the infrared is given by

$$L(\nu) = \int_{\text{envelope}} \rho(r) Q_{\text{abs}}(\nu) B[\nu, T_{\text{g}}(r)] \exp[-\tau(\nu, r)] dV, \quad (1)$$

where $Q_{\text{abs}}(\nu)$ is the absorption efficiency at frequency ν , $\rho(r)$ is the dust grain density, $T_{\text{g}}(\nu)$ is the grain temperature, $B[\nu, T_{\text{g}}(r)]$ is the Planck function, and $\tau(\nu, r)$ is the optical depth at distance r from the centre of the star.

The temperature $T_{\text{g}}(r)$ is determined by the condition of energy balance: amount of energy radiated = amount of energy absorbed. The amount of energy absorbed at any point is proportional to the total available energy at that point, which consists of:

- (i) the attenuated and diluted stellar radiation;
- (ii) scattered radiation, and
- (iii) reradiation from other grains.

Detailed solutions of radiative transfer in circumstellar dust shells by Rowan-Robinson & Harris (1983a,b) indicate that the effect of heating by other grains becomes significant only at large optical depths at the absorbing frequencies [$\tau(\text{UV}) \gg 10$], and at optical depths $\tau(\text{UV}) < 1$ the grains have approximately the same temperature that they would have if they were seeing the starlight unattenuated and no other radiation.

The Planck mean optical depths of circumstellar envelopes around several RV Tauri stars, derived from the ratios of the luminosities of the dust shell (at in-

* E-mail: email@address (AVR); otheremail@otheraddress (ANO)

† This file has been amended to highlight the proper use of \LaTeX 2 ϵ code with the class file. These changes are for illustrative purposes and do not reflect the original paper by A. V. Raveendran.

Table 1. Data on the RV Tauri stars detected by *IRAS*.

| Name Variable | <i>IRAS</i> | Flux density (Jy) ^a | | | | Sp. group | Period (d) | Light- curve type | T_0 (K) |
|------------------|-------------|--------------------------------|------------------|------------------|-------------------|--------------|---------------|-------------------------|-----------|
| | | 12 μm | 25 μm | 60 μm | 100 μm | | | | |
| TW Cam | 04166+5719 | 8.27 | 5.62 | 1.82 | <1.73 | A | 85.6 | a | 555 |
| RV Tau | 04440+2605 | 22.53 | 18.08 | 6.40 | 2.52 | A | 78.9 | b | 460 |
| DY Ori | 06034+1354 | 12.44 | 14.93 | 4.12 | <11.22 | B | 60.3 | | 295 |
| CT Ori | 06072+0953 | 6.16 | 5.57 | 1.22 | <1.54 | B | 135.6 | | 330 |
| SU Gem | 06108+2734 | 7.90 | 5.69 | 2.16 | <11.66 | A | 50.1 | b | 575 |
| UY CMa | 06160–1701 | 3.51 | 2.48 | 0.57 | <1.00 | B | 113.9 | a | 420 |
| U Mon | 07284–0940 | 124.30 | 88.43 | 26.28 | 9.24 | A | 92.3 | b | 480 |
| AR Pup | 08011–3627 | 131.33 | 94.32 | 25.81 | 11.65 | B | 75.0 | b | 450 |
| IW Car | 09256–6324 | 101/06 | 96.24 | 34.19 | 13.07 | B | 67.5 | b | 395 |
| GK Car | 11118–5726 | 2.87 | 2.48 | 0.78 | <12.13 | B | 55.6 | | 405 |
| RU Cen | 12067–4508 | 5.36 | 11.02 | 5.57 | 2.01 | B | 64.7 | | 255 |
| SX Cen | 12185–4856 | 5.95 | 3.62 | 1.09 | <1.50 | B | 32.9 | b | 590 |
| AI Sco | 17530–3348 | 17.68 | 11.46 | 2.88 | <45.62 | A | 71.0 | b | 480 |
| AC Her | 18281+2149 | 41.47 | 65.33 | 21.12 | 7.79 | B | 75.5 | a | 260 |
| R Sct | 18448–0545 | 20.88 | 9.30 | 8.10 | <138.78 | A | 140.2 | a | |
| R Sge | 20117+1634 | 10.63 | 7.57 | 2.10 | <1.66 | A | 70.6 | b | 455 |
| V Vul | 20343+2625 | 12.39 | 5.72 | 1.29 | <6.96 | A | 75.7 | a | 690 |

^a Observed by *IRAS*.

frared wavelengths) and the star, range from 0.07 to 0.63 (Goldsmith et al. 1987). There is much uncertainty in the nature of the optical properties of dust grains in the envelope. The carbon-rich RV Tauri stars are also reported to show the 10- μm silicate emission feature typical of oxygen-rich objects (Gerhz & Ney 1972; Olon & Raimond 1986). The pure terrestrial silicates or lunar silicates are found to be completely unsuitable to account for the infrared emission from circumstellar dust shells around M-type stars (Rowan-Robinson & Harris 1983a). We assume that the absorption efficiency $Q_{\text{abs}}(\nu)$ in the infrared varies as ν^γ . $\gamma = 1$ appears to provide a reasonable fit in a variety of sources (Harvey, Thronson & Gately 1979; Jura 1986). Under these circumstances the condition of energy balance implies that the dust temperature T_g will vary as r^β .

In view of the low value of the observed Planck mean optical depth for the stellar radiation and the nature of the assumed frequency dependence of the absorption efficiency, the extinction of the infrared radiation by the dust envelope can be neglected. If we consider the envelope to be spherically symmetric, equation (1) reduces to

$$L(\nu) = \int_{r_1}^{r_2} 4\pi r^2 \rho(r) Q_{\text{abs}}(\nu) B[\nu, T_g(r)] dr, \quad (2)$$

where r_1 and r_2 are the inner and outer radii of the shell. For a dusty density distribution $\rho(r) \propto r^\alpha$ and $r_2 \gg r_1$, equation (2) reduces to

$$L(\nu) \propto \nu^{2+\gamma-Q} \int_{X_0}^{\infty} \frac{x^Q}{e^x - 1} dx, \quad (3)$$

where $Q = -(\alpha + \beta + 3)/\beta$ and $X_0 = (h\nu/kT_0)$. T_0 represents the temperature at the inner boundary of the dust shell where grains start condensing. In a steady radiation pressure driven mass outflow in the optically thin case, values of α

lie near -2 (Gilman 1972). γ and β are related by $\beta = -2/(\gamma + 4)$.

In the *IRAS* Point Source Catalog (PSC, Beichman et al. 1985a), the flux densities have been quoted at the effective wavelengths 12, 25, 60 and 100 μm , assuming a flat energy spectrum [$\nu F(\nu) = 1$] for the observed sources. For each model given by equation (3), using the relative system response, the colour-correction factors (Beichman et al. 1985b) in each of the *IRAS* passbands were calculated and the fluxes were converted into flux densities expected for a flat energy distribution, as assumed in the *IRAS* PSC, so that the computed colours can be directly compared with the colours determined from the catalogue quantities. Such a procedure is more appropriate than correcting the *IRAS* colours for the energy distribution given by a particular model and then comparing them with those computed by the model.¹

2.1 Colour-colour diagram

The IR colour is defined as

$$[\nu_1] - [\nu_2] = -2.5 \log[f(\nu_1)/f(\nu_2)],$$

where ν_1 and ν_2 are any two wavebands and $f(\nu_1)$ and $f(\nu_2)$ are the corresponding flux densities assuming a flat energy spectrum for the source. In Fig. 1, we have plotted the [25]–[60] colours of RV Tauri stars against their corresponding [12]–[25] colours derived from the *IRAS* data. Filled circles represent stars of group A and open circles stars of group B. The two sets of near-parallel lines represent the loci of constant inner shell temperature T_0 and the quantity Q defined above. The models correspond to the case

¹ An example of a footnote.

Figure 1. Plot of [25]–[60] colours of RV Tauri stars against their [12]–[25] colours after normalizing as indicated in Beichman et al. (1985b). Some of the objects are identified by their variable-star names. Typical error bars are shown in the bottom right-hand corner. The lines represent the loci for constant inner shell temperature and the quantity Q . Note the separation of group A and B stars at $T_0 \sim 460$ K. Positions occupied by a sample of carbon and oxygen Miras are also shown. The $Q = 1.0$ line differs from the blackbody line by a maximum of ~ 0.05 .

of absorption efficiency $Q_{\text{abs}}(\nu)$ varying as ν (with $\gamma = 1$ and hence $\beta = -0.4$). We have omitted R Sct in Fig. 1 because it shows a large deviation from the average relation shown by all the other objects. R Sct has a comparatively large excess at $60 \mu\text{m}$, but the extent of a possible contamination by the infrared cirrus (Low et al. 1984) is unknown. Goldsmith et al. (1987) found no evidence of the presence of a dust envelope at near-IR wavelengths and the spectrum was consistent with a stellar continuum. This explains why R Sct lies well below the mean relation shown by stars of groups A and C between the [3.6]–[11.3] colour excess and the photometrically determined (Fe/H) (Dawson 1979). R Sct has the longest period of 140 d among the RV Tauri stars detected at far-infrared wavelengths and does not have the $10\text{-}\mu\text{m}$ emission feature seen in other objects (Gerhz 1972; Olton & Raimond 1986). R Sct is probably the most irregular RV Tauri star known (McLaughlin 1932).

The inner shell temperatures (T_0) derived for the various objects are also given in Table 1 and we find the majority of them to have temperatures in the narrow range $400\text{--}600$ K. If the dependences of $Q_{\text{abs}}(\nu)$ on ν and $\rho(r)$ on r are similar in all the objects considered, then in the colour-colour diagram they all should lie along a line corresponding to different values of T_0 and in Fig. 1 we find that this is

essentially the case. In view of the quoted uncertainties in the flux measurements, we cannot attach much significance to the scatter in Fig. 1.

At $100 \mu\text{m}$ the infrared sky is characterized by emission, called infrared cirrus, from interstellar dust on all spatial scales (Low et al. 1984), thereby impairing the measurements at far-infrared wavelengths. In Fig. 2, we have plotted the [60]–[100] colours of the six RV Tauri stars detected at $100 \mu\text{m}$ against their [25]–[60] colours, along with the grid showing the regions of different values for inner shell temperature T_0 and the quantity Q , as in Fig. 1. The results indicated by Fig. 2 are consistent with those derived from Fig. 1. AR Pup shows a large excess at $100 \mu\text{m}$ but, in view of the large values for the cirrus flags given in the catalogue, the intrinsic flux at $100 \mu\text{m}$ is uncertain.

2.2 Radial distribution of dust

From Fig. 1, it is evident that all RV Tauri stars lie between the lines corresponding to $Q = 1.5$ and 0.5 . With

$$\alpha = -(1 + Q)\beta - 3,$$

these values suggest limits of $r^{-2.0}$ and $r^{-2.4}$ for the dust density variation, indicating a near-constant mass-loss rate. Jura (1986) has suggested that the density in the circumstellar envelope around RV Tauri stars varies as r^{-1} , implying a mass-loss rate that was greater in the past than it is currently. By fitting a power law to the observed fluxes, such that $f(\nu)$ varies as ν^q , values of q determined by him for the various objects given in Table 1 lie in the range $0.6\text{--}1.2$, with a mean $\bar{q} = 0.98$. The assumption of a power law corresponds to the case of $X_0 = 0$ in equation (3) and hence we get

$$q = 2 + \gamma - Q.$$

Since we assume that $Q_{\text{abs}}(\nu)$ varies as ν , the resulting value for $Q=2.0$. None of the objects is found to lie in the corresponding region in the colour-colour diagram. Even this extreme value for Q implies a density which varies as $r^{-1.8}$.

Goldsmith et al. (1987) have reported that the simultaneous optical and near-IR data of AC Her can be fitted by a combination of two blackbodies at 5680 and 1800 K, representing, respectively, the stellar and dust shell temperatures, and suggested that in RV Tauri stars the grain formation is a sporadic phenomenon and not a continuous process. Apparently, they have been influenced by the remark by Gerhz & Woolf (1970) that their data in the $3.5\text{--}11 \mu\text{m}$ region of AC Her indicated a dust temperature of ~ 300 K. We find that the $K\text{--}L$ colours given by Gerhz (1972), Lloyd Evans (1985) and Goldsmith et al. (1987) are all consistent with each other. Surely, hot dust (~ 1800 K), if present at the time of observations by Goldsmith et al. (1987), would have affected the $K\text{--}L$ colour significantly. AC Her, like other members of its class, is found to execute elongated loops in the ($U\text{--}B$), ($B\text{--}V$) plane (Preston et al. 1963), indicating that significant departure of the stellar continuum from the blackbody is to be expected. Further, their data show only a marginal excess at the near-IR wavelengths. We feel that the case for the existence of hot dust around AC Her and hence for the sporadic grain formation around RV Tauri stars is not strong. In Fig. 3 we find that

Figure 2. Plot of the [60]–[100] colours of RV Tauri stars against their [25]–[60] colours after normalizing as indicated in Beichman et al. (1985b). The solid lines represent the loci for constant inner shell temperature and the quantity Q . The dashed line shows the locus for a blackbody distribution.

AC Her and RU Cen lie very close to R Sct which, according to Goldsmith et al. (1987), shows no evidence for the presence of a hot dust envelope.

2.2.1 Comparison with oxygen and carbon Miras

In Fig. 1 we have also shown the positions of a sample of oxygen-rich and carbon-rich Miras. At the low temperatures characteristic of the Miras, a part of the emission at $12\ \mu\text{m}$ comes from the photosphere. For a blackbody at 2000 K, the ratio of fluxes at wavelengths of 12 and $2\ \mu\text{m}$ (f_{12}/f_2) ~ 0.18 . The Miras shown in Fig. 1 have (f_{12}/f_2) ratios larger than twice the above value. It is clear that the three groups of objects populate three different regions of the diagram. Hacking et al. (1985) have already noticed that there are distinct differences between the *IRAS* colours of oxygen-rich and carbon-rich objects. On the basis of an analysis, using a bigger sample of bright giant stars in the *IRAS* catalogue, this has been interpreted by Zuckerman & Dyck (1986) as being due to a systematic difference in the dust grain emissivity index. U Mon shows the $10\text{-}\mu\text{m}$ silicate emission convincingly and, in most of the other objects for which low-resolution spectra in the near-infrared have been reported (Gerhz 1972; Olon & Raimond 1986), the $10\text{-}\mu\text{m}$ emission may be partly attributed to silicates. Hence it is reasonable to expect that, in the envelopes around at least some of the RV Tauri stars, the dust grains are predominantly of silicates, as in the case of oxygen Miras (Rowan-Robinson & Harris 1983a). The fact that none of the RV Tauri stars is found in the region of the two-colour diagram occupied by the oxygen Miras indicates that the emissivity indices of the silicate grains in the two cases are different. Because of the higher temperatures and luminosities, the environment of grain formation will be different in RV Tauri stars.

2.2.2 Correlation with subgroups

Preston et al. (1963) have identified three spectroscopic subgroups, which are designated as groups A, B and C. Objects of group A are metal-rich; group C are metal-poor; group B

Figure 3. Plot of ($K-L$) colours of RV Tauri stars detected by *IRAS* against their corresponding ($J-K$) colours. The position of AR Pup is indicated. The three objects lying close to the blackbody line are AC Her, RU Cen and R Sct.

objects are also metal-poor, but show carbon enhancements (Preston et al. 1963; Lloyd Evans 1974; Dawson 1979; Baird 1981). It is interesting to see that Table 1 contains no group C objects and that in Fig. 1 there is a clear separation of the two spectroscopic subgroups A and B, with the demarcation occurring at an inner shell temperature of about 450 K, group B stars having lower temperatures than group A. SX Cen is the only exception. Lloyd Evans (1974) has reported that metal lines are stronger in SX Cen than in other group B objects. It may be worth noting that SX Cen has the shortest period among the 100 or so objects with the RV Tauri classification. RU Cen has the coolest inner shell temperature, as already suggested by the near-infrared spectrum (Gerhz & Ney 1972).

Group B objects follow a different mean relationship from those of group A, having systematically larger $11\text{-}\mu\text{m}$ excess for a given excess at $3\ \mu\text{m}$ (Lloyd Evans 1985). For a general sample of RV Tauri stars, the distinction between the oxygen-rich and carbon-rich objects is not that appar-

Landscape figure to go here. This figure was not part of the original paper and is inserted here for illustrative purposes.
See the author guide for details (section 2.2 of `mn2eguide.tex`) on how to handle landscape figures or tables.

Figure 4.

ent in the *JHKL* bands. In Fig. 3 we have plotted the near-IR magnitudes of the objects given in Table 1 (except V Vul which has no available measurements) in the *J-K*, *K-L* plane. The colours, taken from Lloyd Evans (1985) and Goldsmith et al. (1987), are averaged if more than one observation exists, because the internal agreements are found to be often of the order of observational uncertainties, in accordance with the earlier finding by Gerhz (1972) that variability has relatively little effect on colours. Barring RU Cen and AC Her, it is evident that stars belonging to group B show systematically larger excesses at *L* band for a given excess at *K*. The low excesses at near-IR wavelengths for AC Her and RU Cen are consistent with the very low dust temperatures indicated by the far-infrared colours.

It is already well established that from *UBV* photometry one can distinguish between groups A and B, members of group A being significantly redder than those of group B (Preston et al. 1963). Similarly, Dawson (1979) has found that the two spectroscopic groups are well separated in the DDO colour-colour diagrams when mean colours are used for the individual objects.

The clear separation of the spectroscopic subgroups A and B in the IR two-colour diagram suggests that the natures of dust grains in the envelopes in the two cases are not identical. This is to be expected because of the differences in the physical properties of the stars themselves. The average colours of group B stars are bluer than group A, but the envelope dust temperatures of B are cooler than those of A. The near-IR spectra of AC Her and RU Cen are extremely similar (Gerhz & Ney 1972). The striking similarities in the optical spectra of AC Her and RU Cen have been pointed out by Bidelman (O'Connell 1961). We feel that the physical properties, including the chemical composition, of the grains formed in the circumstellar envelope strongly depend on those of the embedded star. This, probably, explains the diversity of the energy distributions of RV Tauri stars in the near-infrared found by Gerhz & Ney (1972). On the basis of the observed differences in chemical abundances and space distribution of RV Tauri stars, Lloyd Evans (1985) has already pointed out that there is no direct evolutionary connection between group A and group B objects, thus ruling out the possibility that group B objects are the evolutionary successors of group A, in which grain formation has stopped and the cooler temperatures for the former are caused by an envelope expansion.

Kukarkin et al. (1969) have subdivided RV Tauri stars into two classes, RVa and RVb, on the basis of their light curves; the former shows a constant mean brightness, whereas the latter shows a cyclically varying mean brightness. Extensive observations in the near-infrared show that, on average, RVb stars are redder than RVa stars, and Lloyd Evans (1985) has suggested that in RVb stars dust shells are denser in the inner regions and hence radiate strongly in the 1–3 μm region. Fig. 3 confirms this; RVb objects show systematically larger (*J-K*) and (*K-L*) colours than RVa objects. Apparently, there is no distinction between objects of the two light-curve types at far-infrared wavelengths (Fig. 1).

3 CONCLUSIONS

In the [12]–[25], [25]–[60] colour diagram, RV Tauri stars populate cooler temperature regions ($T < 600$ K), distinctly different from those occupied by the oxygen and carbon Miras. Using a simple model in which

- (i) the envelope is spherically symmetric,
- (ii) the IR-emitting grains are predominantly of the same kind, and
- (iii) in the infrared the absorption efficiency $Q_{\text{abs}}(\nu) \propto \nu$,

we find that the *IRAS* fluxes are consistent with the density in the envelope $\rho(r) \propto r^{-2}$, where r is the radial distance. Such a dependence for the dust density implies that the mass-loss rates in RV Tauri stars have not reduced considerably during the recent past, contrary to the suggestion by Jura (1986). In the two-colour diagram, the blackbody line and the line corresponding to $\rho(r) \propto r^{-2.2}$ nearly overlap and the present data are insufficient to resolve between the two cases. The latter case is more physically reasonable, however.

The spectroscopic subgroups A and B are well separated in the *IRAS* two-colour diagram, with group B objects having systematically cooler dust envelopes. If we consider only the objects detected by *IRAS*, we find that stars belonging to group B show systematically larger excess at *L* band for a given excess at *K*. Apparently, there is no correlation between the light-curve types (RVa and RVb) and the far-infrared behaviour of these objects. It is fairly certain that the physical properties, including the chemical composition, of the embedded stars are directly reflected by those of the dust grains. Most probably, the grain formation process in RV Tauri stars is continuous and not sporadic as suggested by Goldsmith et al. (1987).

ACKNOWLEDGMENTS

I thank Professor N. Kameswara Rao for some helpful suggestions, Dr H. C. Bhatt for a critical reading of the original version of the paper and an anonymous referee for very useful comments that improved the presentation of the paper.

REFERENCES

- Baird S.R., 1981, *ApJ*, 245, 208
- Beichman C.A., Neugebauer G., Habing H.J., Clegg P.E., Chester T.J., 1985a, *IRAS* Point Source Catalog. Jet Propulsion Laboratory, Pasadena
- Beichman C.A., Neugebauer G., Habing H.J., Clegg P.E., Chester T.J., 1985b, *IRAS* Explanatory Supplement. Jet Propulsion Laboratory, Pasadena
- Dawson D.W., 1979, *ApJS*, 41, 97
- Gerhz R.D., 1972, *ApJ*, 178, 715
- Gerhz R.D., Ney E.P., 1972, *PASP*, 84, 768
- Gerhz R.D., Woolf N.J., 1970, *ApJ*, 161, L213
- Gilman R.C., 1972, *ApJ*, 178, 423
- Goldsmith M.J., Evans A., Albinson J.S., Bode M.F., 1987, *MNRAS*, 227, 143
- Hacking P. et al., 1985, *PASP*, 97, 616
- Harvey P.M., Thronson H.A., Gatley I., 1979, *ApJ*, 231, 115

- Jura M., 1986, *ApJ*, 309, 732
 Kukarkin B.V. et al., 1969, *General Catalogue of Variable Stars*. Moscow
 Lloyd Evans T., 1974, *MNRAS*, 167, 17P
 Lloyd Evans T., 1985, *MNRAS*, 217, 493
 Low F.J. et al., 1984, *ApJ*, 278, L19
 McLaughlin D.B., 1932, *Publ. Univ. Obs. Mich.*, 4, 135
 O’Connell J.K., 1961, *Specola Vaticana Ric. Astron.*, 6, 341
 Olton F.M., Raimond E., 1986, *A&AS*, 65, 607
 Preston G.W., Krzeminski W., Smak J., Williams J.A., 1963, *ApJ*, 137, 401
 Rowan-Robinson M., Harris S., 1983a, *MNRAS*, 202, 767
 Rowan-Robinson M., Harris S., 1983b, *MNRAS*, 202, 797
 van der Veen W.E.C.J., Habing H.J., 1988, *A&A*, 194, 125
 Willems F.J., de Jong T., 1988, *A&A*, 196, 173
 Zuckerman B., Dyck H.M., 1986, *ApJ*, 311, 345

APPENDIX A: LARGE GAPS IN $\text{Ly}\alpha$ FORESTS DUE TO FLUCTUATIONS IN LINE DISTRIBUTION

(This appendix was not part of the original paper by A.V. Raveendran and is included here just for illustrative purposes. The references are not relevant to the text of the appendix, they are references from the bibliography used to illustrate text before and after citations.)

Spectroscopic observations of bright quasars show that the mean number density of $\text{Ly}\alpha$ forest lines, which satisfy certain criteria, evolves like $dN/dz = A(1+z)^\gamma$, where A and γ are two constants. Given the above intrinsic line distribution we examine the probability of finding large gaps in the $\text{Ly}\alpha$ forests. We concentrate here only on the statistics and neglect all observational complications such as the line blending effect (see Harvey et al. 1979, for example).

Suppose we have observed a $\text{Ly}\alpha$ forest between redshifts z_1 and z_2 and found $N - 1$ lines. For high-redshift quasars z_2 is usually the emission redshift z_{em} and z_1 is set to $(\lambda_{\text{Ly}\beta}/\lambda_{\text{Ly}\alpha})(1+z_{\text{em}}) = 0.844(1+z_{\text{em}})$ to avoid contamination by $\text{Ly}\beta$ lines. We want to know whether the largest gaps observed in the forest are significantly inconsistent with the above line distribution. To do this we introduce a new variable x :

$$x = \frac{(1+z)^{\gamma+1} - (1+z_1)^{\gamma+1}}{(1+z_2)^{\gamma+1} - (1+z_1)^{\gamma+1}}. \quad (\text{A1})$$

x varies from 0 to 1. We then have $dN/dx = \lambda$, where λ is the mean number of lines between z_1 and z_2 and is given by

$$\lambda \equiv \frac{A[(1+z_2)^{\gamma+1} - (1+z_1)^{\gamma+1}]}{\gamma+1}. \quad (\text{A2})$$

This means that the $\text{Ly}\alpha$ forest lines are uniformly distributed in x . The probability of finding $N - 1$ lines between z_1 and z_2 , P_{N-1} , is assumed to be the Poisson distribution.

Figure A1. $P(> x_{\text{gap}})$ as a function of x_{gap} for, from left to right, $N = 160, 150, 140, 110, 100, 90, 50, 45$ and 40. Compare this with Lloyd Evans (1985).

A1 Subsection title

We plot in Fig. A1 $P(> x_{\text{gap}})$ for several N values. We see that, for $N = 100$ and $x_{\text{gap}} = 0.06$, $P(> 0.06) \approx 20$ per cent. This means that the probability of finding a gap with a size larger than six times the mean separation is not significantly small. When the mean number of lines is large, $\lambda \sim N \gg 1$, our $P(> x_{\text{gap}})$ approaches the result obtained by Rowan-Robinson & Harris (1983b, fig. 4) for small (but still very large if measured in units of the mean separation) x_{gap} , i.e., $P(> x_{\text{gap}}) \sim N(1-x_{\text{gap}})^{N-1} \sim N \exp(-\lambda x_{\text{gap}})$.

This paper has been typeset from a $\text{T}_{\text{E}}\text{X}/\text{L}^{\text{A}}\text{T}_{\text{E}}\text{X}$ file prepared by the author.

Direct imaging with highly diluted apertures. II: Properties of the point spread function of a hypertelescope

F. Patru^{1,2}, N. Tarmoul¹, D. Mourard¹ and O. Lardière³

¹Laboratoire H. FIZEAU, UMR CNRS 6525 - UNS, OCA - Avenue Copernic, 06130 Grasse, France

²Laboratoire d'Astrophysique de Grenoble (LAOG), 414 Rue de la Piscine, Domaine Universitaire, 38400 Saint-Martin d'Hères, France

³Adaptive Optics Lab, Engineering Lab Wing B133, University of Victoria, PO Box 3055 STN CSC, Victoria, BC, Canada V8W 3P6

Accepted. Received

ABSTRACT

In the future, optical stellar interferometers will provide true images thanks to larger number of telescopes and to advanced cophasing subsystems. These conditions are required to have sufficient resolution elements (resel) in the image and to provide direct images in the hypertelescope mode. It has already been shown (Lardiere et al. 2007) that hypertelescopes provide snapshot images with a significant gain in sensitivity without inducing any loss of the useful field of view for direct imaging applications. This paper aims at studying the properties of the point spread functions of future large arrays using the hypertelescope mode. Numerical simulations have been performed and criteria have been defined to study the image properties. It is shown that the choice of the configuration of the array is a trade-off between the resolution, the halo level and the field of view. A regular pattern of the array of telescopes optimizes the image quality (low halo level and maximum encircled energy in the central peak), but decreases the useful field of view. Moreover, a non redundant array is less sensitive to the space aliasing effect than a redundant array.

Key words: Instrumentation: high angular resolution – Instrumentation: interferometers – Telescopes – Methods: observational

1 INTRODUCTION

Future large interferometers (Labeyrie 2008) need a large number of telescopes and an active cophasing system, to provide images with sufficient sensitivity. If both conditions are met, snapshot imaging can be used in the hypertelescope mode (Labeyrie 1996) and a multi-axial beam combiner seems to be the best solution. If the entrance pupil is highly diluted, the hypertelescope mode improves the Fizeau mode, with a high sensitivity gain without any loss of the useful field of view for direct imaging applications. This useful field, where a direct image can be correctly recovered, is called the Clean Field (Lardiere et al. 2007).

Direct imaging has two main features. In a conventional sense, the goal is to provide snapshot images that could then be post-processed by deconvolution techniques. These images give valuable regularization constraints for the a posteriori astrophysical analysis process. Furthermore, direct imaging is well suitable to feed the entrance plane of focal instruments such as coronagraphic devices or integral field spectrometer. In this paper, we concentrate our analysis on the raw images without considering the deconvolution techniques or the coupling with a focal instrument.

Keeping in mind the researches on the ways to optimize the imaging capabilities of a hypertelescope, this paper aims at characterizing the point spread functions of typical future large arrays. For this purpose, we have developed a numerical simulation, called

HYPERTEL, which first simulates direct images (Sect. 2) and then analyses the densified PSF properties by defining different quantitative criteria (Sect. 3). Then, we study the impact of the array configuration (geometry of the array and number of apertures) and of the recombination mode (Sect. 4). Finally, we establish the relations between the astrophysical parameters of the science object and the main parameters of the hypertelescope (Sect. 5).

2 SIMULATING DIRECT IMAGES

2.1 The input parameters

The input parameters are the wavelength, the characteristics of the science object, the array configuration and the recombination mode.

We assume a perfectly cophased array, without any degradation in the image due to atmospheric turbulence or instrumental bias. To simplify the study, we restrict ourselves to the monochromatic case.

2.1.1 The array configuration

The array is made of N_T identical sub-apertures of index k , defined by their positions $(u_p(k), v_p(k))$ in the input pupil plane and by their diameter d_i . We note s (resp. B) the smallest (resp. largest)

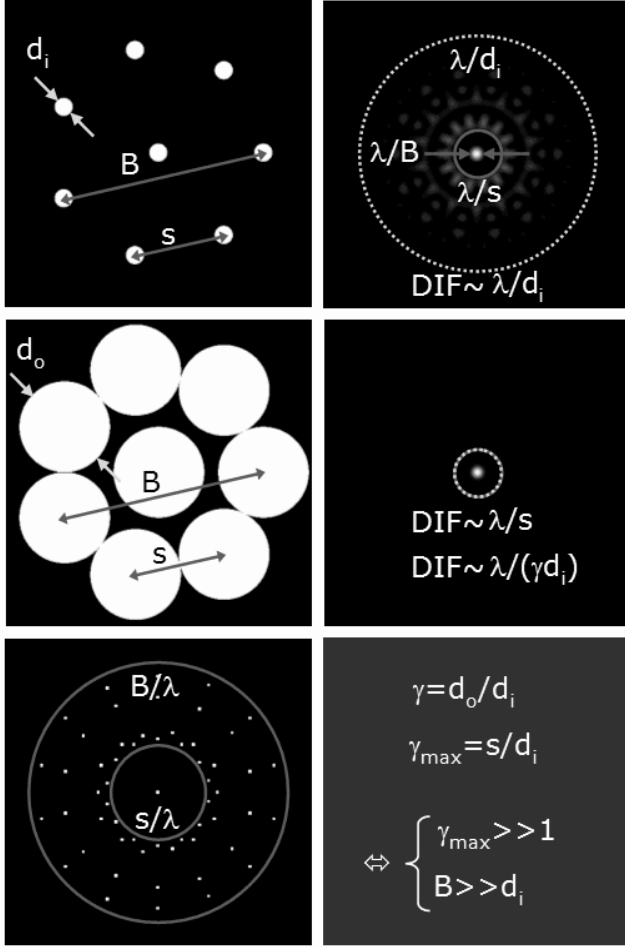


Figure 1. Field of view and direct imaging in hypertelescope mode. An example of an input pupil (top-left) and a densified pupil (middle-left) is shown. We have represented the (u,v) plane coverage (bottom-left) considering that the finite size of the individual telescopes has been neglected. It can be seen that the high spatial frequencies are distributed over the interval $[s/\lambda, B/\lambda]$, with s the smallest baseline and B the largest baseline of the array. The maximum densification factor γ_{max} equals to s/d_i (bottom-right). The Fizeau (top-right) and densified (middle-right) point spread functions (PSF) are shown. As predicted, we observe a central peak inside a clean zone, called the Clean Field (*CLF*), where the contribution of the side-lobes'halo is minor (see (Lardiere et al. 2007) for the different definitions of fields). It is surrounded by a non-negligible halo of speckles outside the *CLF* diameter ($CLF = \lambda/s$). The Fizeau PSF is limited by the Airy envelope of an input sub-aperture, which corresponds to the coupled field ($CF = \lambda/d_i$). The pupil densification reduces the Direct Imaging Field (DIF) to match the CLF. The central peak is intensified by a factor γ^2 .

baseline of the array. The maximum angular resolution of the array, following the Rayleigh criterion, is given by the highest baseline :

$$resel \simeq \frac{\lambda}{B} \quad (1)$$

2.1.2 The science object

The object is defined by a monochromatic brightness map, N_{pxl} pixels wide. The angular extent of this map is equal to the object

diameter θ_{obj} . The angular size of a pixel θ_{pxl} , i.e. the smallest angular element seen on the sky, should respect the Shannon criterion:

$$\theta_{pxl} = \frac{\theta_{obj}}{N_{pxl}} < \frac{resel}{2} \quad (2)$$

In practice, we choose $\theta_{pxl} < resel/6$.

Thus, $N_{pxl} > \frac{6B}{\lambda} \cdot \theta_{obj}$.

The object is considered as composed of elementary incoherent sources, corresponding to the N_{pxl}^2 pixels of the brightness map. Each elementary source of index m is defined by its coordinates $(X_{obj}(m), Y_{obj}(m))$ and by its intensity $I_{obj}(m)$.

For each elementary source, the off-axis position is defined on the two axis by:

$$\begin{aligned} \theta_{X_{obj}(m)} &= \left(X_{obj}(m) - \frac{N_{pxl}}{2} \right) \theta_{pxl} \\ \theta_{Y_{obj}(m)} &= \left(Y_{obj}(m) - \frac{N_{pxl}}{2} \right) \theta_{pxl} \end{aligned} \quad (3)$$

The image is obtained as the sum of the sub-images of each incoherent elementary source. As the input sub-pupils are very diluted, we neglect the variation of the object in the spatial frequency domains $[\frac{B-d_i}{\lambda}; \frac{B+d_i}{\lambda}]$ accessible in certain recombination schemes.

2.1.3 The recombination mode

Pupil densification increases by a factor γ the relative size of the beams and keeps the relative positions of the sub-pupil centres (Fig. 1). This pseudo-homothetic transformation does not affect the interferometric pattern in the image and correctly recovers the high resolution information. The diffraction envelope is reduced, so as to concentrate all the flux in the useful field.

The alternative concept of IRAN (Vakili et al. 2004a) combines the beams by superimposing the images of the sub-pupils with small tilts in the image plane. A direct image is obtained in the recombined pupil plane.

The envelope shape is a Bessel function in Pupil Densification (DP mode) and is a flat field in IRAN mode. The envelope width decreases as the densification factor increases. The value of the latter is chosen between 1 (Fizeau mode) and γ_{max} (maximum densification).

The maximum densification factor depends on the smallest baseline s and on the aperture diameter d_i :

$$\gamma_{max} = \frac{s}{d_i} \quad (4)$$

The pupil densification amplifies the intensity of the signal by a factor γ^2 . In the IRAN mode, the densification factor can not be larger than $\gamma_{max}/2$ due to the diffraction of the sub-pupils (Lardiere et al. 2007). Thus the sensitivity gain is reduced by a factor 4 and the DIF is enlarged by a factor 2, compared to the DP mode.

We mainly focus in this paper on the pupil densification (DP) for the recombination mode. We also make comparison with the image densification (IRAN).

2.2 The image calculation

The principle of the image calculation is schematically described in Fig. 2. In the image plane, each pixel of coordinates (x, y) has an intensity of $I(x, y)$.

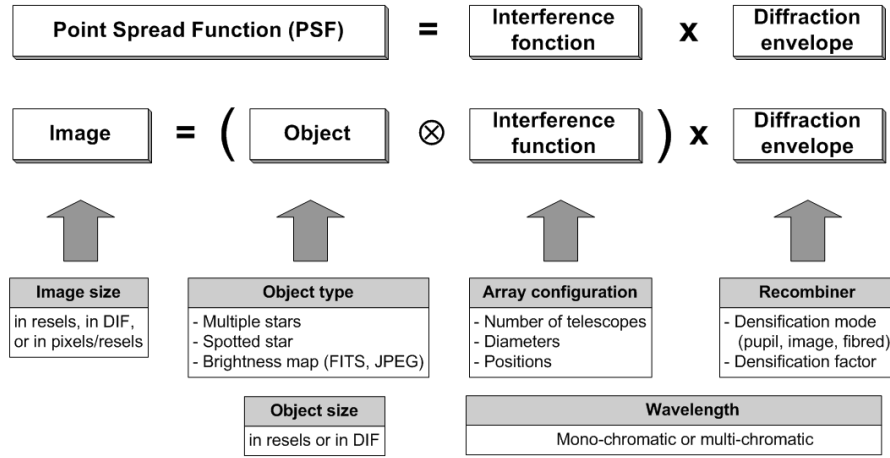


Figure 2. Main structure of HYPERTEL. The Point Spread Function is defined as the product of the interference function with the diffraction envelope. The direct image is defined as the convolution of the object brightness distribution by the interference function, the result being multiplied by the diffraction envelope.

The Point Spread Function (Lardiere et al. 2007) is defined as the product of the interference function $I_0(x, y)$ (function of the array pattern) with the diffraction envelope $A_0(x, y, \gamma)$ (function of the recombination mode and of the densification factor).

$$I_{PSF}(x, y) \approx A_0(x, y, \gamma) \times I_0(x, y), \quad (5)$$

with:

$$I_0(x, y) = \left| \sum_{k=1}^{N_T} e^{-\frac{2i\pi}{\lambda}(x \cdot u_p(k) + y \cdot v_p(k))} \right|^2 \quad (6)$$

The direct image of an astrophysical object is defined as the object brightness distribution $O(\theta_{X \text{ obj}}, \theta_{Y \text{ obj}})$ convolved by the interference function, the result being multiplied by the diffraction envelope.

$$I(x, y) \approx A_0(x, y, \gamma) \cdot O(\theta_{X \text{ obj}}, \theta_{Y \text{ obj}}) \otimes I_0(x, y) \quad (7)$$

Finally, the image computed by HYPERTEL is the sum of the sub-images of each incoherent elementary source of the object (as defined in Sect. 2.1.2).

$$I(x, y) = A_0(x, y, \gamma) \cdot \left| \sum_{k=1}^{N_T} e^{-\frac{2i\pi}{\lambda}(x \cdot u_p(k) + y \cdot v_p(k))} \cdot \sum_{m=1}^{N_{pxl}} I_{obj}(m) \cdot e^{\frac{2i\pi}{\lambda}\psi(m, k)} \right|^2 \quad (8)$$

We denote $\psi(m, k)$ the phase delay seen by the k^{th} sub-aperture due to the position of the elementary source m . Indeed each elementary source is seen under a different angle by each sub-aperture of the interferometer. Hence, $\psi(m, k)$ is given by:

$$\psi(m, k) = \theta_{X \text{ obj}}(m) \cdot u_p(k) + \theta_{Y \text{ obj}}(m) \cdot v_p(k) \quad (9)$$

3 DEFINITION OF THE CHARACTERISTICS OF THE POINT SPREAD FUNCTION (PSF)

3.1 Input and output pupils' parameters

As the computed images are a function of the characteristics of the entrance pupil, we first define two parameters related to the interferometer configuration. The entrance (resp. densified) pupil filling rate τ_i (resp. τ_o) is defined as the ratio between the total surface area of the input (resp. output) pupil and the surface area of an input (resp. output) sub-pupil, d_i (resp. d_o) being the diameter of the latter:

$$\tau_i = \frac{S_{input \text{ sub-pupils}}}{S_{input \text{ pupil}}} = N_T \frac{d_i^2}{(B + d_i)^2} \quad (10)$$

$$\tau_o = \frac{S_{output \text{ sub-pupils}}}{S_{output \text{ pupil}}} = N_T \frac{d_o^2}{(B + d_o)^2} = N_T \left(\frac{\gamma d_i}{B + \gamma d_i} \right)^2 \quad (11)$$

3.2 Field of view parameters

The definitions of the different fields of view for a hypertelescope have been extensively studied by (Lardiere et al. 2007). We just recall here the important definitions of these different fields. We distinguish the CLean Field of view (CLF), the Direct Imaging Field of view (DIF) and the Coupled field of view (CF). They are illustrated on figure 1.

$$CLF = \frac{\lambda}{s} \text{ (radians)} = \frac{B}{s} \text{ (resels)} \quad (12)$$

$$DIF \simeq \frac{\lambda}{(\gamma - 1) d_i} \quad (13)$$

$$CF = \frac{\lambda}{d_i} \quad (14)$$

The Clean Field is physically related to the sampling of the (u, v) plane and according to Nyquist-Shannon sampling theorem, it is defined by the smallest baseline s . This definition is also interesting on calculating the number of resels in the Clean Field.

The coupled field (CF) is imposed by the size of a sub-aperture. The Direct Imaging Field (DIF) depends on the densification mode. The DIF width is still obviously smaller than the CF width.

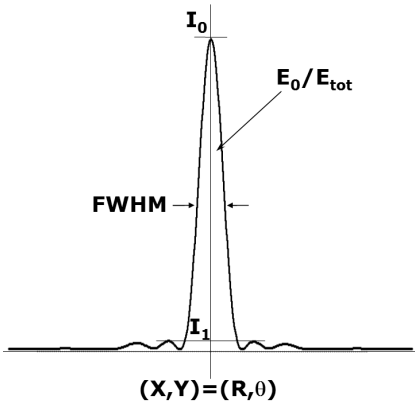


Figure 3. Imaging parameters of the densified point spread function. Coordinates $((X, Y) = (R, \theta))$, on-axis intensity (I_0), encircled energy (E_0/E_{tot}), full-width at half-maximum ($FWHM$) of the central peak, maximum halo level (I_1/I_0).

3.3 Astrometric criteria

In the direct image, the position of each interference peak (central peak and side-lobes) is given by the coordinates of its photocentre (Fig. 3). The full width at half maximum ($FWHM$) of the central peak corresponds to the smallest resolution element (resel), given by equation 1. It characterizes the sharpness of the image. It depends not only on the wavelength and on the maximum baseline, but also on the geometry of the array.

3.4 Photometric criteria

The on-axis intensity I_0 is equal to the height of the central peak. The encircled energy is defined as the ratio of the fraction of energy contained in the central peak E_0 to the total energy in the image E_{tot} :

$$\frac{E_0}{E_{tot}} = \frac{2\pi}{E_{tot}} \int_0^{\theta_0} I(\rho) \rho d\rho \quad (15)$$

where θ_0 corresponds to the first minimum from the center of the field (Fig. 3).

3.5 Halo level criteria

We also define a criterion to estimate the contribution of the halo surrounding the central peak. The maximum of the halo level is defined as the ratio between I_1 the intensity of the highest side-lobe inside the CLF and I_0 the intensity of the central peak (Fig. 3).

$$\text{Maximum halo level} = \frac{I_1}{I_0} \quad (16)$$

4 DENSIFIED PSF PROPERTIES

4.1 Influence of the array geometry

4.1.1 Presentation of the simulations

We consider four typical array configurations, made of 40 telescopes, 10m in diameter and distributed over a maximum baseline of 1km with $\lambda=0.6\mu\text{m}$. The distribution of the pupils is taken from

ELSA (Quirrenbach 2004), OVLA (Labeyrie et al. 1986), KEOPS (Vakili et al. 2004b) and CARLINA (Labeyrie et al. 2003). Figure 4 and Table 1 give the characteristics of the PSFs and compare the cases of pupil densification (DP mode) and image densification (IRAN mode (Vakili et al. 2004a)).

OVLA and ELSA have an almost uniform coverage of the (u,v) plane and a large clean field (10 and 18 resels respectively). OVLA has diffraction rings and ELSA has diffraction spikes inside the clean field, so that only 12% of the energy is contained inside the central peak. The maximum halo level corresponding to the diffraction structures reaches 16% (resp. 22%) of the amplitude of the central peak for OVLA (resp. ELSA).

KEOPS and CARLINA have a uniform coverage of the input pupil, so that the coverage of the output pupil is maximized. The densified pupil filling rate reaches 75% (resp. 69%) for KEOPS (resp. CARLINA). The minimal distance between the telescopes is also optimized, so that the clean field is reduced to about 5 resels. The advantage is an improvement of the image quality, so that the encircled energy reaches 71% (resp. 65%) for KEOPS (resp. CARLINA), whereas the maximum halo level remains below 3%.

4.1.2 Trade-off between halo level and field of view

For a given resolution, it appears that, depending on the chosen configuration, there is a trade-off between halo level and field of view. OVLA is suitable to image large fields, since the corresponding diffraction envelope (dashed line) has a large full width at half maximum. KEOPS and CARLINA are optimized for high contrast imaging, thanks to a regular distribution of the telescopes of the array.

The condition to reach a low halo level with a monolithic telescope is to have an aperture without obstruction, or to use apodization techniques (Aime and Soummer 2003a). In these conditions, the (u,v) plane coverage has a conic shape. In a similar way, the (u,v) plane of an interferometer used for high contrast imaging must be identical. It has been shown that the optimization of the filling of the (u,v) plane is obtained by maximizing the integral of the squared modulus of the Modulation Transfer Function (Aime and Soummer 2003b). It consists in fact in maximizing the densified pupil filling rate τ_o (Eq. 11), by a regular distribution of the sub-pupils.

4.1.3 Trade-off between resolution and field of view

For a given configuration, it appears also that there is a trade-off between resolution and field. If one increases the global size of the input pupil (B) with a constant number of apertures, the resolution is improved whereas the clean field is decreased. A compact array provides a large image with low resolution and a diluted array provides a sharp image with high resolution. It is interesting to benefit from a movable array with a fixed geometry like KEOPS and with a sufficient number of telescopes. With a small number of iterations, the telescopes could be moved keeping the same geometry so as to finally adapt the Clean Field to the typical dimension of the object.

4.2 Impact of the number of apertures

4.2.1 Presentation of the simulations

We now consider the same four array configurations but with a variable number of telescopes (up to 100) of diameter 10m distributed over a constant maximum baseline of 1km.

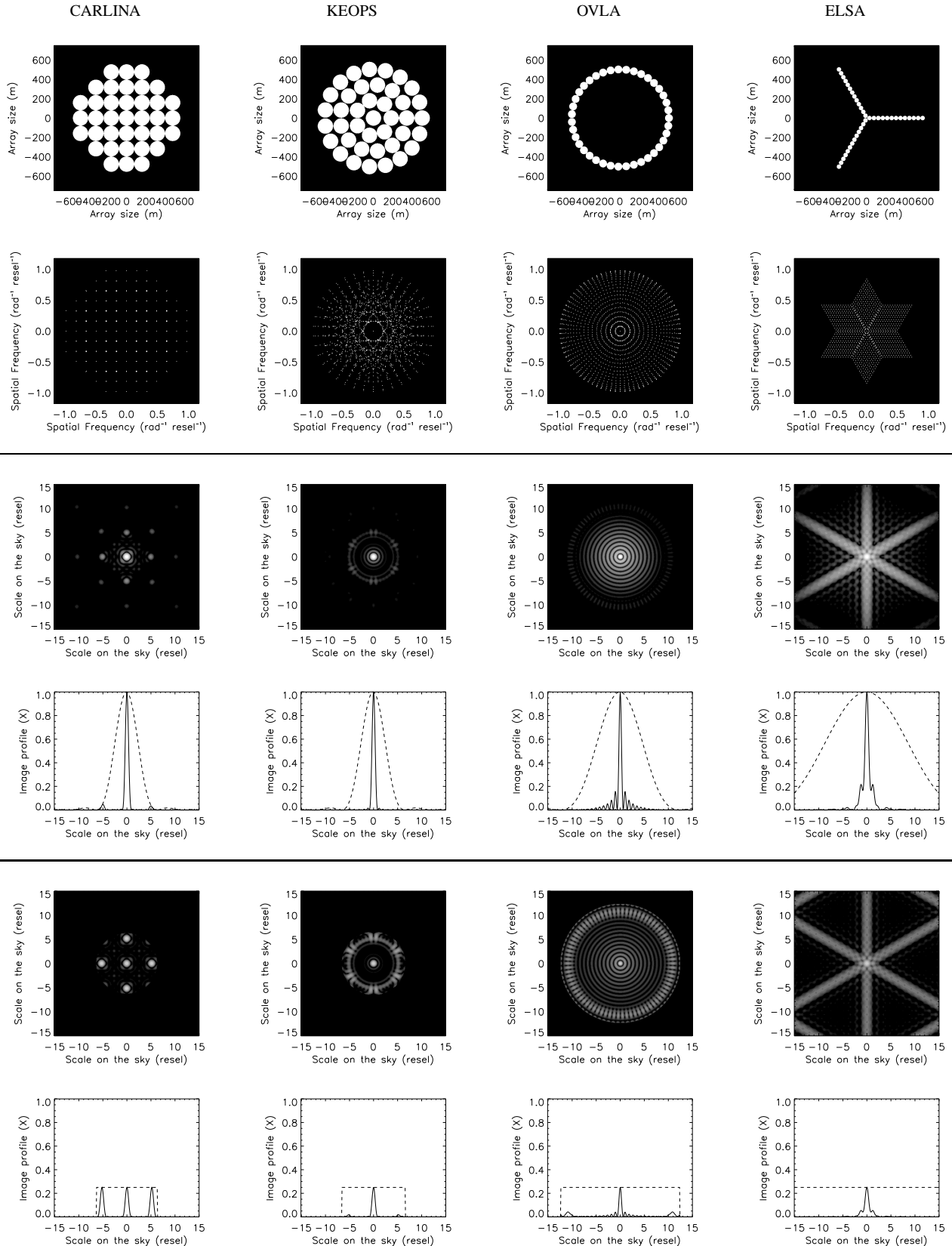


Figure 4. Imaging properties of 4 array configurations of 40 telescopes. The apertures with a diameter of $10m$ are laying out on an entrance pupil with an external diameter of $1km$. From top to bottom: Densified output pupil, (u,v) plan coverage, image (logarithmic scale) and profile of the PSF in DP mode, image and profile of the PSF in IRAN mode. The dashed lines represent the profile of the diffraction envelope, its edge corresponds to the CLean Field extent. The intensities in the images are normalized to 1 for the central resel of each densified image in DP mode. Due to a lower densification factor in the IRAN mode ($\gamma_{max}/2$), the intensity of the central peak is only $1/4$.

| | | CARLINA-37 | KEOPS-40 | OVLA-39 | ELSA-39 |
|--------------------------------------|----------------|------------|----------|---------|---------|
| Entrance pupil filling rate | τ_i | 3.6e-3 | 3.9e-3 | 3.8e-3 | 3.8e-3 |
| Densified pupil filling rate | τ_o | 0.69 | 0.75 | 0.22 | 0.07 |
| Maximum densification level | γ_{max} | 15.8 | 15.8 | 8.1 | 4.4 |
| Clean field [mas] | CLF | 0.78 | 0.78 | 1.54 | 2.79 |
| Clean field [resel] | CLF | 5.18 | 5.18 | 10.18 | 18.45 |
| Direct imaging field [resel] | DIF | 5.53 | 5.53 | 11.62 | 23.82 |
| FWHM of the central peak [resel] | $FWHM$ | 0.73 | 0.70 | 0.55 | 0.89 |
| Encircled energy of the central peak | E_0/E_{tot} | 0.71 | 0.65 | 0.12 | 0.12 |
| Maximum halo level in the CLF | I_1/I_0 | 0.03 | 0.02 | 0.16 | 0.22 |

Table 1. Imaging parameters of 4 array configurations of 40 telescopes. The aperture diameters are equal to $10m$ and the maximum baseline is $1km$, so that the *resel* is $0.12 mas$ and the Coupled Field *CF* is $82 resels$.

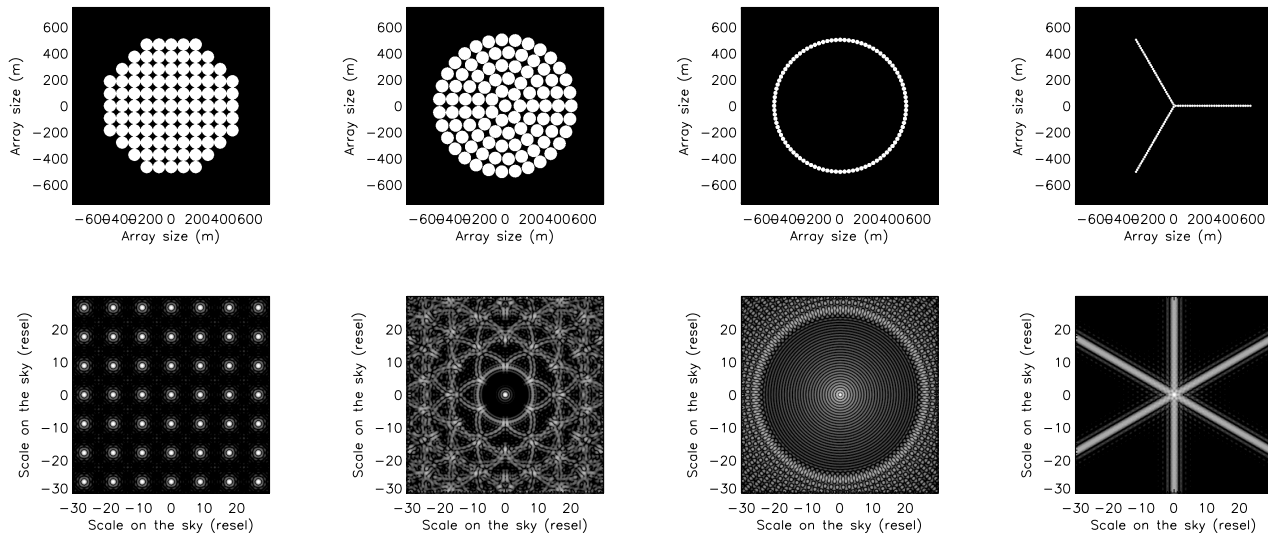
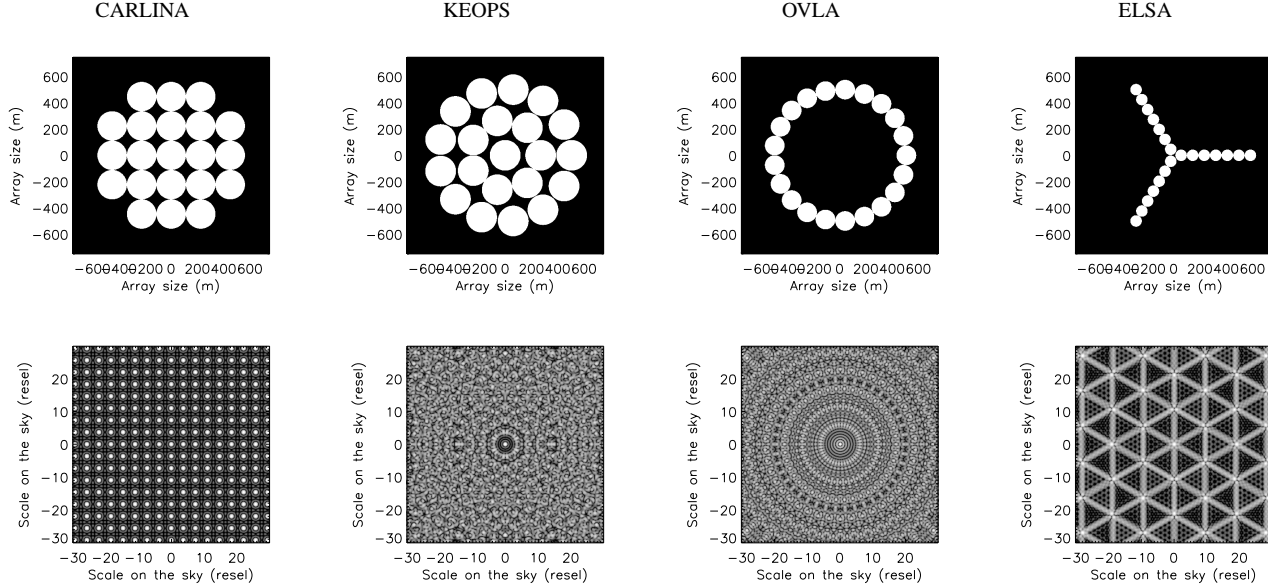


Figure 5. Imaging properties of 4 array configurations with N_T telescopes. Densified pupil and interference function (logarithmic scale) as defined in Eq. 6 with an array of $N_T \simeq 20$ apertures (top) and $N_T \simeq 100$ apertures (bottom). The apertures with a diameter of $10m$ are laying out on an entrance pupil with an external diameter of $1km$. For these images, the intensity is normalized to the maximum on-axis intensity ($I_0 = 1$).

| | | KEOPS-8 | KEOPS-21 | KEOPS-40 | KEOPS-65 | KEOPS-96 |
|--------------------------------------|----------------|---------|----------|----------|----------|----------|
| Entrance pupil filling rate | τ_i | 0.78e-3 | 2.1e-3 | 3.9e-3 | 6.4e-3 | 9.4e-3 |
| Densified pupil filling rate | τ_o | 0.76 | 0.75 | 0.75 | 0.75 | 0.74 |
| Maximum densification level | γ_{max} | 44.5 | 23.3 | 15.8 | 12.0 | 9.6 |
| Clean field [mas] | CLF | 0.28 | 0.53 | 0.78 | 1.03 | 1.28 |
| Clean field [resel] | CLF | 1.84 | 3.52 | 5.18 | 6.83 | 8.49 |
| Direct imaging field [resel] | DIF | 1.88 | 3.67 | 5.53 | 7.46 | 9.47 |
| <hr/> | | | | | | |
| Full-width half-maximum [resel] | $FWHM$ | 0.56 | 0.66 | 0.70 | 0.72 | 0.74 |
| Encircled energy of the central peak | E_0/E_{tot} | 0.66 | 0.67 | 0.69 | 0.72 | 0.73 |
| Maximum halo level (inside the CLF) | I_1/I_0 | 0.03 | 0.02 | 0.02 | 0.02 | 0.02 |
| <hr/> | | | | | | |
| | | OVLA-9 | OVLA-21 | OVLA-39 | OVLA-69 | OVLA-96 |
| Entrance pupil filling rate | τ_i | 0.88e-3 | 2.1e-3 | 3.8e-3 | 6.7e-3 | 9.4e-3 |
| Densified pupil filling rate | τ_o | 0.60 | 0.36 | 0.22 | 0.13 | 0.10 |
| Maximum densification level | γ_{max} | 34.8 | 14.9 | 8.1 | 4.6 | 3.3 |
| Clean field [mas] | CLF | 0.36 | 0.83 | 1.54 | 2.72 | 3.78 |
| Clean field [resel] | CLF | 2.36 | 5.48 | 10.18 | 18.0 | 25.1 |
| Direct imaging field [resel] | DIF | 2.43 | 5.88 | 11.62 | 23.1 | 36.1 |
| <hr/> | | | | | | |
| Full-width half-maximum [resel] | $FWHM$ | 0.53 | 0.55 | 0.55 | 0.55 | 0.55 |
| Encircled energy of the central peak | E_0/E_{tot} | 0.42 | 0.20 | 0.11 | 0.07 | 0.05 |
| Maximum halo level (inside the CLF) | I_1/I_0 | 0.13 | 0.16 | 0.16 | 0.16 | 0.16 |

Table 2. Imaging parameters of the configurations KEOPS (upper part) and OVLA (lower part) as a function of the number of telescopes. The aperture's diameter is 10m and the maximum baseline 1km, so that the *resel* is 0.12 mas and the Coupled Field *CF* is 82 *resels*.

In order to keep the geometry of each configuration, we use the following principles for computing the different arrays:

- ELSA : at each step, we add one telescope on each arm of the Y, starting at 3 telescopes, then 6 and up to 99.
- OVLA : at each step, 1 telescope is added on the ring with a diameter of 1 km, starting at 2 telescopes, then 3 and up to 100. The telescopes are regularly distributed in azimuth.
- KEOPS : we start with a telescope at the centre and one concentric ring of 7 telescopes. Then we add successively concentric rings made of 13, 19, 25 and 31 telescopes. The array is successively composed of 8 (1 ring), 21 (2 rings), 40 (3 rings), 65 (4 rings) and 96 (5 rings) telescopes. The diameter of the largest ring always equals 1 km.
- CARLINA : at each step, the array is build with n^2 telescopes regularly distributed over a square grid, with n from 2 to 11. The telescopes outside the circle of diameter B are removed. The array is composed successively of 4, 9, 12, 21, 32, 37, 52, 69, 80 and 97 telescopes.

The intensity is normalized by the collecting surface area of each array so that the sensitivity considered here is independent of the number of telescopes.

4.2.2 PSF quality parameters

Figure 5 shows the densified pupils and the interference function (as defined in Eq. 6) of the four configurations with 20 and 100 telescopes. Figure 6 and Table 2 give the evolution of the main parameters of the arrays as a function of the number of telescopes. Figure 7 gives the evolution of the densified PSF parameters as a function of the number of telescopes for each configuration. Figure 8 shows the correlation between the PSF parameters and the densified pupil filling rate.

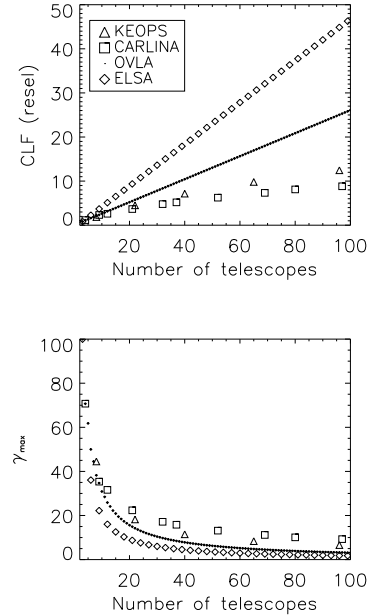


Figure 6. Clean Field (top) and densification level (bottom) of arrays as a function of the number of telescopes.

Whatever the number of telescopes, CARLINA and KEOPS benefit from a quasi-complete densified pupil filling rate, so that their imaging properties (inside the clean field) are very close to a monolithic telescope. The encircled energy in the central peak contains about 70% of the luminous energy and the contribution of the halo remains below 3% inside the clean field. CARLINA and KEOPS are a priori equivalent in term of image quality, regarding to the halo level and the encircled energy.

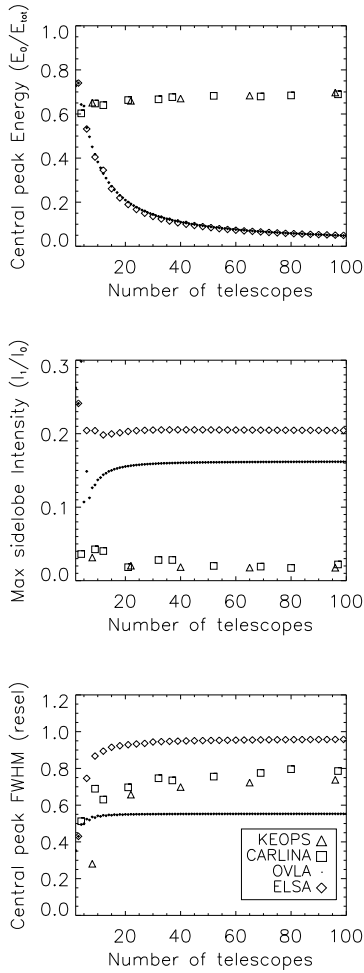


Figure 7. PSF parameters in DP mode as a function of the number of telescopes. From top to bottom: Encircled energy, the maximum halo level, the FWHM of the central peak

For OVLA and ELSA, the output pupil shape is similar whatever the number of telescopes. When the number of telescopes increases in these arrays, the densification level remains low due to the shortest baselines. The encircled energy in the central peak falls from 40% to only 5%, regarding the configurations from 10 to 100 telescopes. The halo level is not negligible for ELSA (20%) and OVLA (15%).

The sharpness of the image is characterized by the FWHM of the central peak. The narrowest peak is provided by OVLA, thanks to the huge central obstruction of the input pupil. ELSA exhibits strong diffraction spikes but the PSF looks very sharp in the other position angles. For KEOPS and CARLINA, the FWHM of the central peak increases slowly with the number of telescopes.

5 BIASES INDUCED ON THE PSF

In the previous section, we have studied various configurations of future arrays. This study has allowed us to characterize them with quantitative parameters. It appears clearly that, whatever the configuration, the imaging properties will be degraded by difficulties

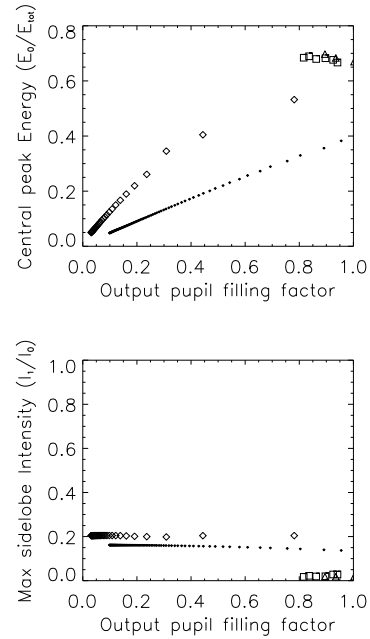


Figure 8. Encircled energy (top) and the maximum halo level (bottom) of the densified PSF in DP mode as a function of τ_o . B is constant and N_T increases as on Fig. 6 or Fig. 7. The symbols represent the different configurations as on Fig. 6 or Fig. 7.

in restoring the photometric parameters in the field. Three main effects are identified:

- the bias of the interference function,
- the space aliasing effect,
- the bias of the diffraction envelope.

The two first depend on the array configuration, whereas the last bias is only related to the recombination mode.

5.1 Bias of the interference function

The photometric parameters of a source are biased by the halo of the interference function (as defined in Eq. 6), which induces a contrast loss in the image. The quality of the interference function of the array is simply related to the actual shape of the entrance pupil.

If the input sub-pupils are distributed regularly, the densified pupil is almost complete, and the halo inside the clean field reproduces the diffraction pattern of a large monolithic telescope covering all the sub-pupils. If the densified pupil shows gaps, additional diffraction figures are added to first ones.

Thus, the halo is minimized by maximizing the densified pupil filling rate τ_o , with a regular pattern of the sub-apertures in the entrance pupil.

5.2 Space aliasing effect

The space aliasing effect (Aime 2008) appears in the direct image when the science object is surrounded by sources outside the clean field but inside the coupled field, or when the science object diameter is larger than the clean field. Besides, all the sources in the CF will contribute to the central image but only the sources in the CLF will form a correct central peak plus a halo of sidelobes,

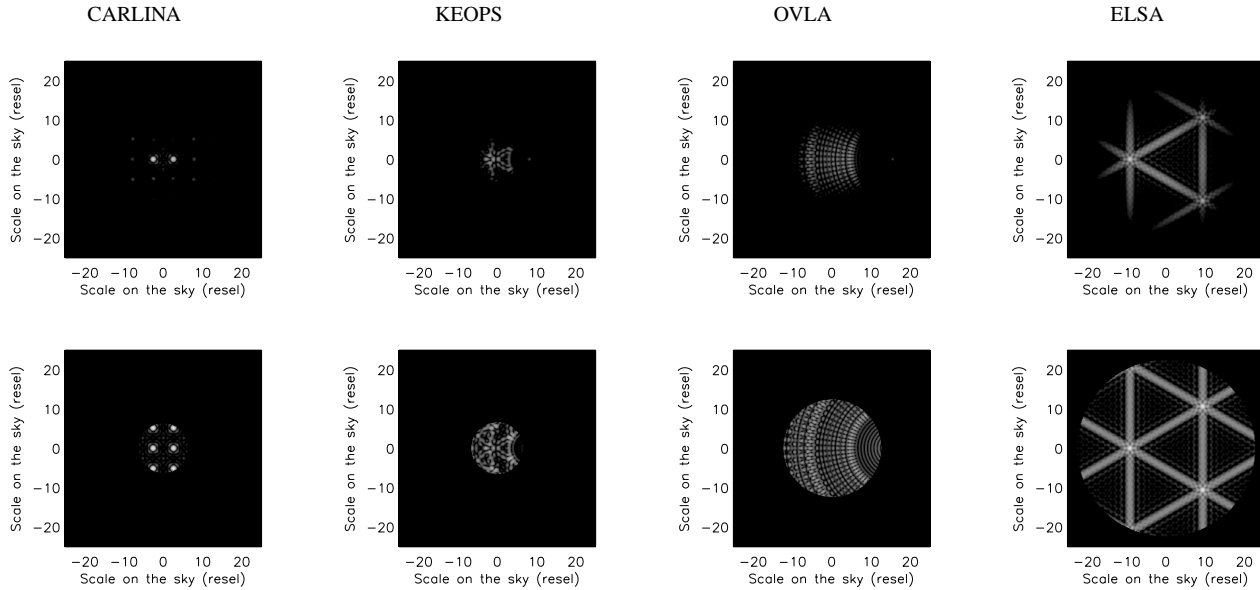


Figure 9. Image (logarithmic scale) of an off-axis star simulated for 4 array configurations with 40 telescopes in DP mode (up) and in IRAN mode (down). The off-axis position equals to 1.5 times the CLean Field, so that the star is outside the CLean field and inside the Coupled Field. Due to the space aliasing effect, one or several ghost stars appear if the array configuration is redundant (CARLINA and ELSA), contrary to the non redundant cases (KEOPS and OVLA).

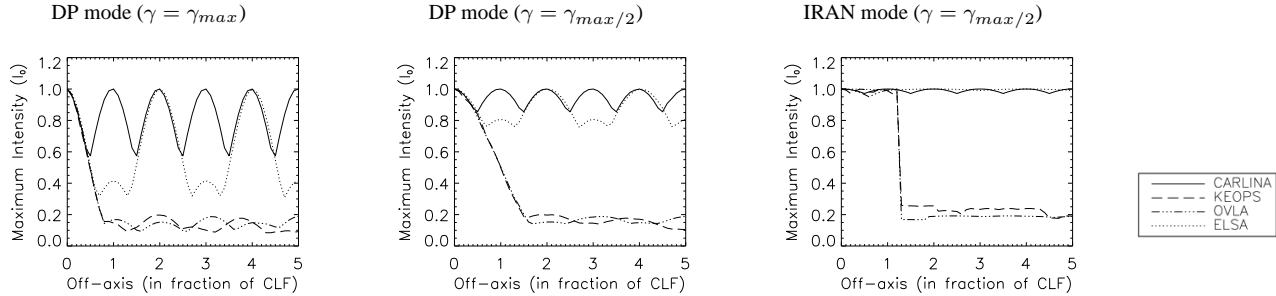


Figure 10. Evolution of the maximum intensity in the CLean Field as a function of the radial position of an off-axis star. The intensity has been normalized to 1 when the star is on-axis, so that the intensity in $DP_{\gamma_{max}}$ mode (left) is in practice 4 times higher than $DP_{\gamma_{max}/2}$ mode (middle) and IRAN mode (right). If the off-axis star equals to $CLF/2$, the intensity reach respectively 0.50, 0.85 and 1 for the 3 modes (left to right), due to the diffraction envelope in DP mode (no effect in IRAN mode). If the star is outside the CLF, a redundant array (CARLINA and ELSA) induces replication of the main lobe in the CLF. A non redundant array (KEOPS and OVLA) only induces a diffused halo lower than 0.25 in the CLF.

whereas the sources in the CF and outside the CLF will just form a halo of sidelobes. These side-lobes induce photometric perturbations locally distributed in the image.

Redundant arrays are more affected by the space aliasing effect than non redundant arrays. Indeed, a redundant array provides an interference function with high level parasit peaks, whereas a non redundant one has a smooth interference function. In the image formation, these differences in the interference functions will introduce important space aliasing effects as shown on Fig. 9 and 10.

In the redundant case, a source in the Coupled Field but outside the Clean Field provides ghost images inside the Clean Field. In the non redundant case, the same star will only induce a diffused halo reducing the contrast in the Clean Field.

5.3 Bias of the diffraction envelope

Due to the diffraction envelope contribution, the quality of the photometry restitution decreases from the axis to the edge of the clean field (Fig. 10). A partial densification restitutes a more homogeneous photometry in the clean field, but decreases the sensitivity gain. This bias does not exist in IRAN mode, where the envelope is flat.

5.4 Discussion

The main effects on the PSF can be theoretically corrected by image restoration or deconvolution. Deconvolution techniques are required for complex objects. In the case of a densified image, the problem is that the convolution relationship is lost. The image and the PSF are in fact partially truncated, which is a problem for the classical methods of deconvolution. To overcome this prob-

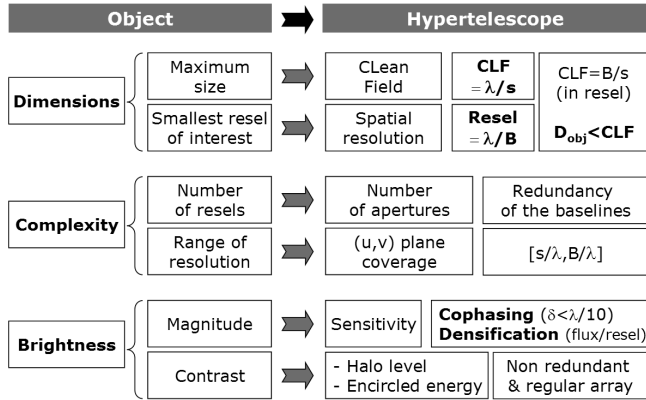


Figure 11. Instrumental parameters of a hypertelescope vs astrophysical parameters of the science object.

lem, a hybrid method, based on likelihood maximization, reconstructing simultaneously the object and the PSF has been proposed (Aristidi et al. 2006).

Figure 11 gives the links between the science object and the hypertelescope's required characteristics. An astrophysical object is characterized by its dimensions, its complexity and its brightness. These characteristics are linked to the main parameters of a hypertelescope: field, resolution, pupil pattern.

The main dimensions of the object are the external diameter and the smallest resel of interest. The maximum size of the object should not exceed the diameter of the clean field, which leads to the value of the minimum baseline of the array ($CLF = \lambda/s$). The smallest resel corresponds to the required resolving power, which imposes the largest baseline B of the array ($resel = \lambda/B$). The clean field can also be expressed in number of resels ($CLF = B/s$).

The complexity of the object determines the required number of resels in the image, the number of telescopes and the array geometry. The other aspect to be considered is the resolution range of the object on the interval $[\lambda/B, \lambda/s]$.

The limiting magnitude of an array is directly related to the performances of the cophasing device, allowing long exposures. The image quality (highest encircled energy in the central peak and lowest halo level in the Clean Field) is directly related to the densified pupil filling rate.

6 CONCLUSION

Simulations have shown that the choice of the array configuration (array pattern and number of apertures) is a trade-off between the resolution, the halo level and the useful field. The spatial resolution is given by the largest baseline ($resel = \lambda/B$). The clean field is a function of the smallest baseline ($CLF = \lambda/s$). The halo level and the encircled energy in the central peak are a function of the densified pupil filling rate τ_o . The sine qua none condition to image a complex source without space aliasing effect is that the object diameter should not exceed the clean field width ($\theta_{obj} < \lambda/s$).

Concerning the beam combiner, it has been shown that the maximum densification is optimal in term of sensitivity, by equalizing the direct imaging field (DIF) with the clean field.

Simulations have shown that the configurations KEOPS and CARLINA are equivalent as regards the image characteristics.

However, KEOPS is less sensitive to the space aliasing effect, contrary to CARLINA where ghost stars are introduced by the pollution of the surrounding sources. Thus, a non redundant array is required for Direct Imaging to minimize the space aliasing effect.

Finally, the best configuration seems to be the one proposed by KEOPS, which has a regular and non redundant layout of the telescopes. This configuration provides the best quality of the interference function, in comparison with the interference function of the equivalent giant telescope. Indeed, it provides the lowest halo level (inside the Clean Field), at the limit of the diffraction of such kind of array. Moreover, minimizing the halo level improves the signal to noise ratio, which should simplify the deconvolution process.

Thus, a KEOPS configuration seems to be suited for high-contrast imaging of compact sources. An OVLA configuration can be used for wide field imaging, providing a larger clean field and the best resolving power.

This paper was mainly focused on future large arrays with a large number of sub-apertures. However, the direct imaging technique already has a great interest for current operating interferometers, using an efficient cophasing system. Indeed, the densification may provide the ultimate sensitivity.

It will be also interesting in the future to compare the performances of direct imaging and aperture synthesis. The introduction of the fundamental and instrumental noises is also mandatory for a correct evaluation of the scientific performances. Finally this work will be developed in two main directions: the study of the instrumental performances of direct imaging arrays when coupled with integral field spectrometers or coronagraphs, and the comparison of the practical imaging performances of various array configurations when deconvolution is applied.

ACKNOWLEDGMENTS

The authors wish to thank the referee, Chris Haniff, for important suggestions and clarifications.

REFERENCES

- Aime C. and Soummer R. 2003, Astronomy with High Contrast Imaging, EAS Publications Series, 8, 79
- Aime C. and Soummer R. 2003, Astronomy with High Contrast Imaging, EAS Publications Series, 8, 353
- Aime C. 2008, A&A, 483, 361
- Aristidi E., Vakili F., Schutz A. et al. 2006, EAS Publications Series, 22, 103
- Labeyrie A., Koechlin L. and Lemaitre G. 1986, Proc. SPIE, 628, 323
- Labeyrie A., 1996, A&AS, 118, 517
- Labeyrie A., Le Coroller H., Dejonghe J. et al. 2003, Proceedings SPIE Hawaii 4852, 236-247
- Labeyrie, A., 2008, "ELTs, interferometers and hypertelescopes at different wavelengths", proc. "ELTs at different wavelengths", SPIE Lund, in press
- Lardièrè O., Martinache F. and Patru F. 2007, Mon. Not. R. Astron. Soc. 375, 977
- Patru F. et al. 2007, MNRAS, 376, 1047
- Quirrenbach A. 2004, Science cases for next generation optical/infrared interferometric facilities (the post VLTI era), Proc. of the 37th Liege International Astrophys. Colloquium, 43
- Vakili F., Aristidi E., Abe L. and Lopez B. 2004, A&A, 421, 147

Vakili F., Belu A., Aristidi E. et al. 2004, Proc. SPIE, 5491, 1580